The Effect of Engine Location on the Aerodynamic Efficiency of a Flying-V Aircraft

Rubio Pascual, Berta; Vos, Roelof

DOI
10.2514/6.2020-1954

Publication date
2020

Document Version
Final published version

Published in
AIAA Scitech 2020 Forum

AIAA SciTech Forum
6-10 January 2020, Orlando, FL
AIAA Scitech 2020 Forum

10.2514/6.2020-1954

The Effect of Engine Location on the Aerodynamic Efficiency of a Flying-V Aircraft

Berta Rubio Pascual* and Roelof Vos†
Delft University of Technology, Delft, 2629 HS, the Netherlands

The Flying-V is a novel flying wing concept where the main lifting surface has been fully integrated with the passenger cabin. This study focuses on the effect of engine positioning on aerodynamic interference under regulatory and structural constraints. An initial benchmark for the lift-to-drag ratio is obtained from a baseline Flying-V configuration, and the influence of the x, y and z position, as well as engine orientation are subsequently analysed. An Euler solver on a three-dimensional, unstructured grid is used to model the flow at cruise condition: $M = 0.85$, $h = 13,000$ m, $\alpha = 2.9°$, and a thrust per engine of 50 kN. The viscous drag contribution is computed using an empirical method. A total of forty different engine locations are tested under these conditions to build a surrogate model that predicts the aircraft's lift-to-drag ratio based on the position of the engine. The results obtained show that misplacing the engine can lead to significant lift-to-drag ratio losses going as high as 55% when compared against the ideal integration configuration. A region behind the airframe's trailing edge is identified where the interference losses due to the installation are minimized. At this location, engine installation causes a 10% penalty in aerodynamic efficiency, a minimum one-engine-inoperative yawing moment and a small thrust-induced pitching moment.

Nomenclature

Latin Symbols

c	=	chord (m)
C_F	=	friction coefficient (∼)
C_L	=	lift coefficient (∼)
C_D	=	drag coefficient (∼)
C_p	=	pressure coefficient (∼)
d	=	inter-engine distance (m)
E	=	volume-specific power (J/s/m^3)
g	=	constraint function (∼)
h	=	altitude (m)
K	=	drag-polar parameter (∼)
L	=	lift (N)
m	=	mass (kg)
M	=	Mach number (∼)
p	=	pressure (N/m^2)
r	=	radius (m)
R	=	gas constant (J/kg/K)
S	=	momentum source term (N/m^3)
T	=	thrust (N)
U	=	speed (m/s)
$\vec{v}$	=	velocity vector
V	=	volume (m^3)
x, y, z	=	Cartesian coordinates (m)

Greek Symbols

α	=	angle of attack (deg)
β	=	geometric angle (deg)
γ	=	ratio of specific heats (∼)
ϕ	=	force in x-dir. (N)
ρ	=	density (kg/m^3)
Ψ	=	spread angle (deg)
θ	=	impact angle (deg)
ξ, η, ζ	=	non-dimensional coordinates (∼)

Subscripts

0	=	zero lift
AF	=	airframe
axim	=	azimuth
f	=	friction or fan
ff	=	fan face
hi	=	highlight
inv	=	inviscid
i	=	integer

*Student, Faculty Aerospace Engineering
†Assistant Professor, Faculty of Aerospace Engineering, r.vos@tudelft.nl, Associate Fellow AIAA

LE	=	leading edge
long	=	longitudinal
nac	=	nacelle
pre	=	pre-entry streaam
ref	=	reference
T	=	total
th	=	throat

Acronyms

CFD	=	computational fluid dynamics
DOE	=	design of experiments
CRM		Common reference model
CST		class shape transformation
KBE	=	knowledge-based engineering
LHS	=	latin hypercube sampling
FV	=	Flying V
SU2	=	Stanford University Unstructured
TFN		through-flow nacelle

I. Introduction

Since many years, flying-wing aircraft have been regarded as a promising way to reduce both drag and structural weight. Already during the Second World War this idea began to sink in, as the absence of fuselage and horizontal tail was expected to result in a very low zero-lift drag coefficient.[1] From that moment on, countless designs of flying wings (FW), flying fuselages, and blended-wing-bodies (BWB) have been studied in order to take advantage of the diverse predicted benefits in terms of aerodynamic and structural behaviour.[2] Now that the classical tube-and-wing configuration can no longer be further optimized, flying-wing aircraft have become an important asset to reduce the climate impact of long-haul aircraft.[3,4]

The Flying-V concept originated in 2015 as part of this trend: a novel aircraft configuration where the main lifting surface has been fully integrated with the passenger cabin. This new layout was originally developed by Benad[5] as a result from a collaboration between TU Berlin and Airbus GmbH, and studied in more depth by Faggiano et al.[6] and Van der Schaft.[7] All these studies showed that the Flying-V is characterized by a significant potential to save fuel due to its increased lift-to-drag ratio when compared to traditional tube-and-wing aircraft .[8] In these studies, however, the positioning of the engines and their integration was not investigated. It has been shown that engine positioning can have a great impact in the aerodynamic efficiency of an aircraft.[9] Therefore, the aim of this study is to investigate the effect of the engine positioning on the lift-to-drag ratio of the Flying-V, while respecting constraints with respect to structural integration and regulations.

Figure 1: Conceptual design of the Flying V

Engine integration on flying-wing aircraft has been conducted before. Studies can be found that range from multidisciplinary design processes that aim to improve the aerodynamic performance of a model,[10] to more synergistic integration proposals that aim to reduce the environmental impact of the aircraft.[11] Engine integration studies have been performed for BWB,[12,13] and FW[14] showing that apart from the traditional turbofan integration, one could also opt for a more distributed propulsion system.

The objective of this study, however, is limited to finding an adequate location, and orientation for the Flying-V twin turbofan engines. To address this at the level of the design process, the following assumptions are made. On the one hand, the integration study is performed for cruise conditions, that is $h = 13000$ [m], $M = 0.85$, and $\alpha = 2.9°$, following the ones considered by Faggiano et al. in Ref.[8] Besides, for the purpose

of comparability with this work, all aerodynamic coefficients presented here have been made nondimensional using a reference area of $S = 895$ m^2. Based on the drag coefficient obtained for the clean configuration and the thrust provided by the A350 engines, it is assumed that each engine provides a thrust of T = 50 kN. No pylon is included in the investigation either, given the current stage of the Flying-V design, and neither are the winglets. Furthermore, only over-the-wing configurations are taken into account for this integration study as it is envisioned that the pylon structure and undercarriage support structure are integrated to reduce structural weight.

The remainder of the paper is organized as follows: In Section II, the design methodology is explained. Section III introduces the validation and verification processes used, and in Section IV the simulation results are shown and discussed. Finally, the conclusions of this project and some future lines of work are discussed in Section V.

II. Methodology

Four main parameters are investigated due to their relevance from an engine integration point of view: the engine's x, y and z coordinates, and its orientation. In a nutshell, the design approach can be divided in three phases as depicted in Figure 2: problem definition, aerodynamic simulations and analysis. First, the figure of merit that will be used to determine if a certain position is "adequate" or not is chosen based on the main advantages that the Flying-V configuration brings along from an aerodynamic point of view. Then, to properly define a design space where it would be reasonable to position the engine, additional constraints are imposed to account for aspects other than the purely aerodynamic ones, which are also of key importance when carrying out an engine integration study. Subsequently, prior to running any aerodynamic simulations, the set of points inside the design space to be investigated is chosen using a Design of Experiments (DoE). A limited number of different engine locations are tested on the Flying-V. To better understand the impact of each parameter on the final result, a preliminary surrogate model is built which relates the aerodynamic behavior of the aircraft to the position of the engines. Finally, based on the results obtained, a region is defined where the location of the engine better fulfills the imposed requirements; and within this region, a final engine location is proposed for which a final battery of tests at several angles of attack are carried out.

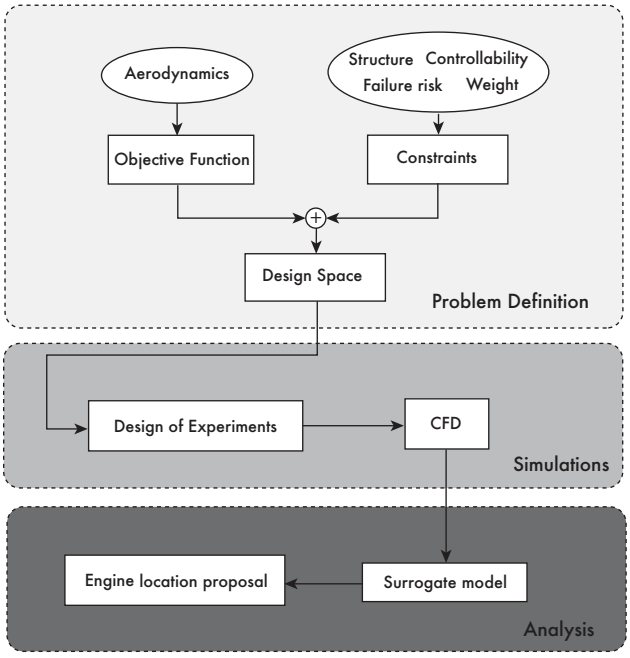

Figure 2: Overview of the design methodology followed for the engine-integration study for the Flying-V

II.A. Design Objective

There are many parameters to be observed in order to understand the impact of installing an engine on an airframe, but in this case, the "adequacy" of a certain engine location is determined by the impact of the positioning parameters on the lift-to-drag ratio at a fixed angle of attack ($\alpha = 2.9°$) and a fixed set of cruise conditions. The design space is limited to account for key integration aspects such as structural feasibility, center-of gravity location, and regulatory requirements. It is worth mentioning that obtaining accurate values for the lift-to-drag ratio in power-on condition with the available CFD tools has proven to be a challenging task. Therefore, a "baseline" lift-to-drag ratio is defined so that perturbations due to engine positioning can be compared against this reference value.

II.B. Design Space Definition

The task of finding both a good location and orientation for the engines is tackled as a two-step approach. First, the influence of the three spatial coordinates is observed by testing a set of ten preliminary locations with constant engine orientation (toe angle and incidence both zero). The idea behind this initial investigation of the available design space is to gain insight on the capabilities of the analysis method to capture the aerodynamic phenomena observed in different regions of the design, and to refine the design space based on the results. Then, once the final design space is spatially bounded, forty different locations are simulated and analyzed to build the surrogate model. Then, for two of the sampled locations an orientation study is performed where the toe angle of the engine is varied.

The sampling points are chosen using *pyDOE's* latin-hypercube-sampling (LHS) algorithm. The only input that LHS requires is the number of sampled locations. The algorithm then outputs a set of dimensionless coordinates that parametrize the location of the different samples inside the design space. Hence, the first step in the design process is to define the design space to be sampled. From now onwards, this zone is called the *feasible region*, and it encompasses the area surrounding the Flying-V where it would be reasonable to locate the engines. The term *reasonable* in this case refers to the ability to fulfill the requirements imposed to the structural, regulatory, and control aspects.

To position the engine and its nacelle, the center of the circular intake face is chosen as a reference point. Figures 3a and 3b show the considered design space for this reference point in the form of a colored parallelepiped. The yellow boundaries are set in order to ensure the structural feasibility of the configuration: the engine cannot be located too far away from the wing, as otherwise too large of a pylon would be needed, bringing along significant weight penalties. As a rule of thumb, it is established that the distance between the lower face of the nacaelle and the suction side of the wing cannot be more than 1 meter apart, and the engine's reference point cannot be more than 3.5 meters behind the wing's trailing edge, measured in x-direction. In principle, the lowest height allowed for the engine should be that which places the engine as close to the airframe as possible as long as they do not intersect with one another. After the preliminary analysis of the design space, however, it was detected that a small channel between both bodies can lead to the formation of strong shockwaves, ($M \approx 1.8$), which' effect cannot be well predicted when using an Euler solver. Hence, the lower yellow line indicates the chosen lower bound for the engine position. The purple line (3a) and blue line (3b) are set to ensure that the engine intake is positioned in an area of subsonic flow, where the undisturbed flow is decelerating with increasing chordwise position.

The green line limiting the maximum distance of the engines from the symmetry plane is set as a rule of thumb to 11.4 meters. It is thought that an engine position further outboard would require too large of a vertical tail and rudder to balance one-engine inoperative yawing moments.

II.C. Minimum Inter-Engine Spacing

To prevent catastrophic failure in case of turbine or compressor disk failure, the engines need to be laterally spaced to limit this probability. The current regulation,[15] establishes a minimum safety distance between engines (and other critical components) to provide protection in the event of disk turbine failure. Hence, three design practices should be taken into account: critical systems or components should be located outside the likely debris impact areas, these systems should either be duplicated or provided with suitable protection in case one or several of the aforementioned components are indeed located within the impact areas, and this protection should be provided by the use of airframe structure or additional shielding. These recommendations have been proved effective to mitigate hazards within the $\pm 15°$ impact area.

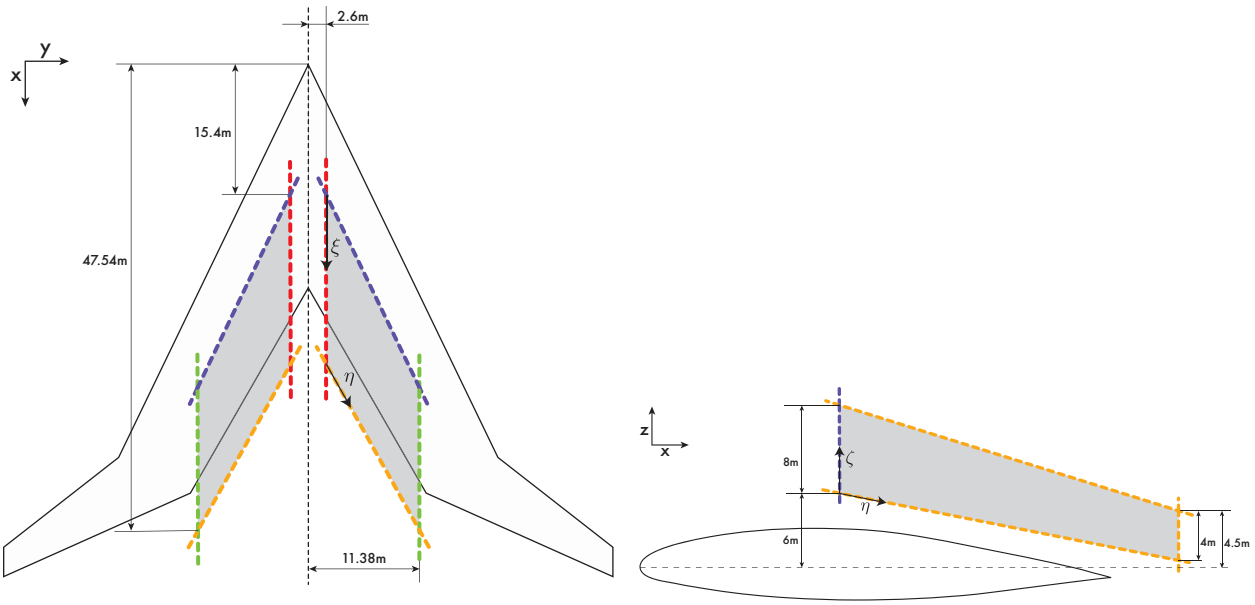

(a) Top view of the allowed engine region

(b) Section-AA of the allowed engine region

Figure 3: Allowed engine region. The non-dimensional parameters used to the define the engine location in that area are given by: ξ, η, and ζ coordinates respectively

Based on the approach usually followed in preliminary aircraft design studies, and provided that it is not yet known where most of the aforementioned critical systems would be located on the Flying-V, it is reasonable to only investigate the minimum required distance at which both engines should be positioned from each other. The risk of impact depends on two main parameters: the longitudinal (θ_{long}), and azimuth (θ_{azim}) spread angles of the debris (see Figures 4a and 4b), which can be expressed as follows:

$$\theta_{\text{azim, 1}} = \arctan\left(\frac{l_{\text{nac, 1}}}{d}\right) \qquad \theta_{\text{azim, 2}} = \arctan\left(\frac{l_{\text{nac, 2}}}{d}\right) \tag{1}$$

$$\theta_{\text{long}} = \arctan\left(\frac{r_{\text{max}}}{d}\right). \tag{2}$$

Since in this case the main focus of the study is on the engines, the blue area represents how a turbine blade "sees" the other engine. The pink region indicates the spread angle of the blade in each direction, which for the case of the azimuth is fixed to a certain Ψ which varies depending on the specific component being considered.[15] The probability, p, of impact for each case is obtained by dividing the blue angle by the pink one:

$$p_{\text{azim}} = \frac{2\theta_{\text{azim, 1}}}{\Psi} + \frac{2\theta_{\text{azim, 2}}}{\Psi} \tag{3}$$

$$p_{\text{long}} = \frac{\theta_{\text{long}}}{2\pi} \tag{4}$$

Note that Ψ is the highest value that the sum of both azimuth angles can reach. The total probability of impact as a function of the engine distance is then:

$$p_{\text{tot}} = p_{\text{long}} \cdot p_{\text{azim}}. \tag{5}$$

In Figure 5, the probability of impact in each direction along with the total probability of impact is plotted. The dotted black line presents the regulatory constraint at a risk of 5%, ensuring a 95% probability of non-catastrophic disk failure. As can be seen, the engines can be positioned 5 meters apart in order to satisfy this regulation. This boundary is also reflected in Fig. 3a.

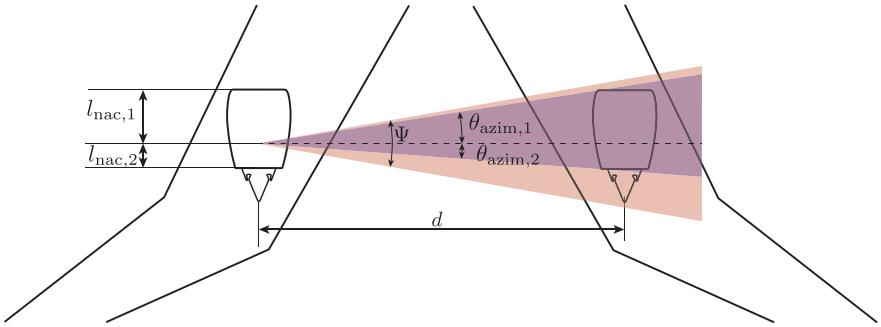

(a) Wing plane

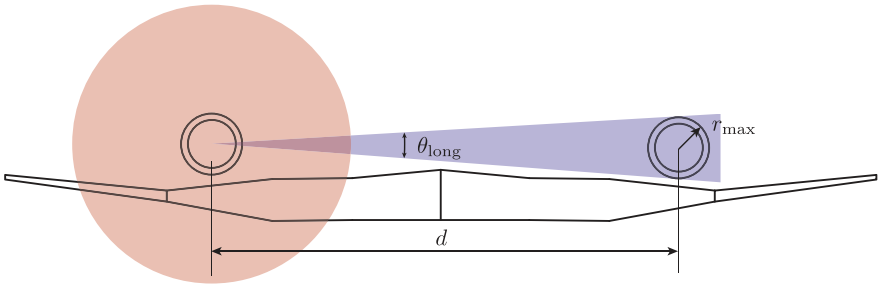

(b) Disk plane

Figure 4: Geometrical representation of the engine failure risk assessment

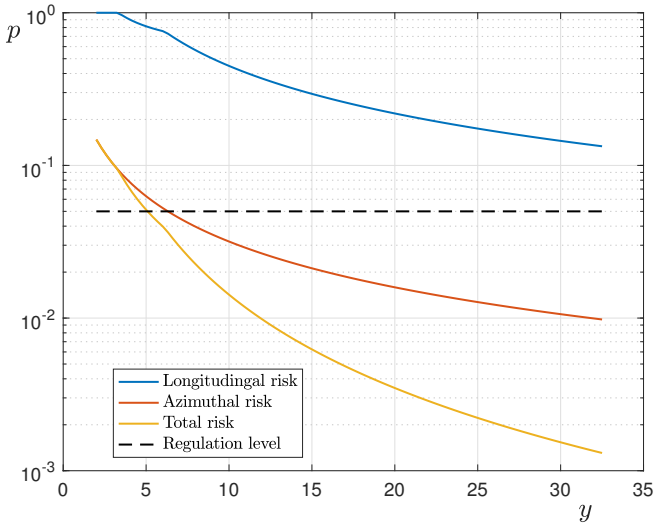

Figure 5: Total probability of impact after disk turbine failure as a function of the engine distance

II.D. Sampling the Design Space

Once the boundaries of the design space are properly defined, the number of sampled points is chosen. In the case at hand, 40 different engine positions are deemed sufficient using latin hyper-cube sampling (LHS), as they provide a reasonable coverage of the feasible region while including points close to the edges. The LHS algorithm, however, only provides the non-dimensional coordinates used to parameterize the region of interest (ξ, η, ζ). These are subsequently converted to the Cartesian coordinates (x, y, z) which define the position of the engine with respect to the leading edge of the wing section in the symmetry plane. The following equations relate the non-dimensional coordinates plotted in Figure 6 to the Cartesian coordinates:

$$x = \xi(c_y + \Delta_{c0} + \Delta_{cf}) + x_{LE} - \Delta_{c0} \tag{6}$$
$$y = [\eta(\delta_{b0} + \delta_{bf} + 1) - \delta_{b0}]b/2 \tag{7}$$
$$z = \Delta_z + \zeta h_z \tag{8}$$

where,

$$h_z = h_{z_{\max}} + m(x - c_0) \tag{9}$$
$$\Delta_z = \Delta_{z,\max} + h_{min} + r_{\max} + mx - c_0 \tag{10}$$

and

$$m = (h_{\min} - h_{\max})/(c_f - c_0), \tag{11}$$

with

$$c_0 = x_{LE} - \Delta_{c0} \tag{12}$$
$$c_f = x_{LE} + c_y + \Delta_{c0} \tag{13}$$

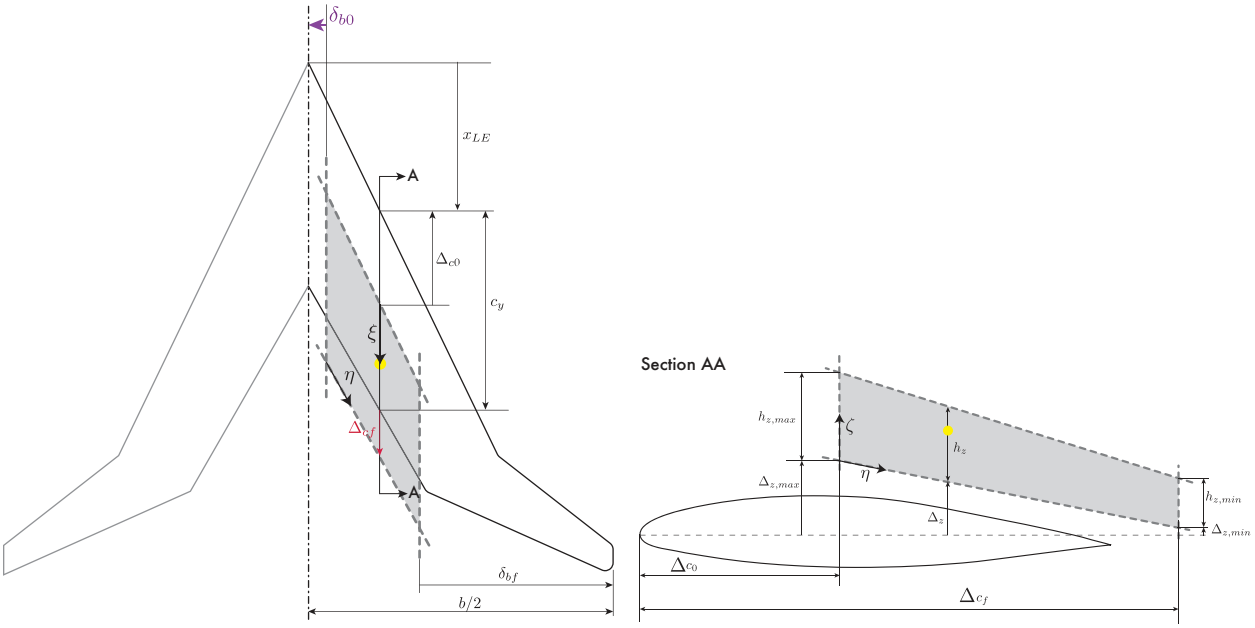

(a) Top view of the allowed engine region and engine position parameterization within the design space

(b) Section-AA of the allowed engine region and the engine position parameterization within the design space

Figure 6: Detail of the engine position parameterization on the allowed engine region

II.E. Model set-up

The geometric model of the Flying-V with engines is created using ParaPy, a Knowledge Based Engineering (KBE) framework. The main KBE program consists of two modules: Multi Model Generator (MMG) and

PyEngine (PE). The former is in charge of creating the Flying-V geometry for a set of parameters, while the latter is generating the engine cowling as defined by a set of geometrical constraints. The output of these two modules is then fed to the *Engine-Airframe* module, which integrates both geometries following the directives of an external input file. An overview of the program layout is presented in Figure 7. Once the integrated model is generated, the meshing module comes into action to mesh the computational domain that encompasses both bodies. The Flying-V airframe model chosen is the one that resulted from the dual step optimization carried out by Faggiano et al.[8]

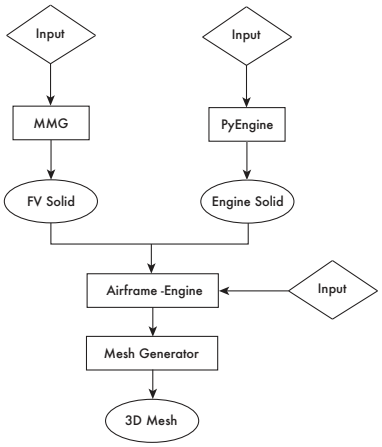

Figure 7: Code diagram showing the model set-up

Regarding the shape of the nacelle, it is clear that when studying the aerodynamic interaction between engine and airframe, the specific nacelle geometry plays a very important role. Nevertheless, given the early stage of the Flying-V design, the specific engine geometry has not been fixed yet. Since the main goal of this project is the positioning of the engine, it is is deemed reasonable to use a standard nacelle geometry to model the Flying-V engine, and put off its design optimization for future work. The preliminary design methodology for nacelles based on CST curves proposed in Ref.[16] is used. This solution consists of a parametric approach to define the geometry of the turbofan nacelle by specifying 6 parameters of its geometry, and a set of constraints. This is not only used to generate the outer shape of the nacelle, but also for the inlet lip. The remaining section (inner walls of the exhaust region) are defined by giving a fixed set of data points which depend on the overall geometry of the nacelle. These points are extracted from the original CAD files of the NASA Common Research Model (CRM).

Following the procedure detailed by Christie et al. in,[17] the geometry parameters used to define the outer cowling surface and inlet lip are shown in Figure 8. The constraints imposed for each contour are presented in the following equations referring to the nomenclature of Fig. 8:

$$\text{Cowling constraints:} \begin{cases} g_{1c} = r_{\max}/r_{\text{hi}} \\ g_{2c} = l_{\text{nac}}/r_{\text{hi}} \\ g_{3c} = f_{\text{if}} \\ g_{4c} = (r_{\text{te}} - r_{\text{hi}})/l_{\text{nac}} \\ g_{5c} = \theta_{\text{nac}} \end{cases} \tag{14}$$

$$\text{Inlet constraints:} \begin{cases} g_{1i} = (2r_{\text{hi}} - r_{\text{i}_{\text{th}}})/r_{\text{hi}} \\ g_{2i} = l_{\text{in}}/r_{\text{hi}} \\ g_{3i} = f_{\max_i} \\ g_{4i} = (r_{\text{hi}} - r_{\text{fan}})/l_{\text{in}} \\ g_{5i} = \beta_{\text{ff}} \end{cases} \tag{15}$$

Even though the CRM nacelle model has been conceived for a conventional under-the-wing configuration, it serves as a benchmark since its design cruise condition is similar to the Flying-V. The external shape,

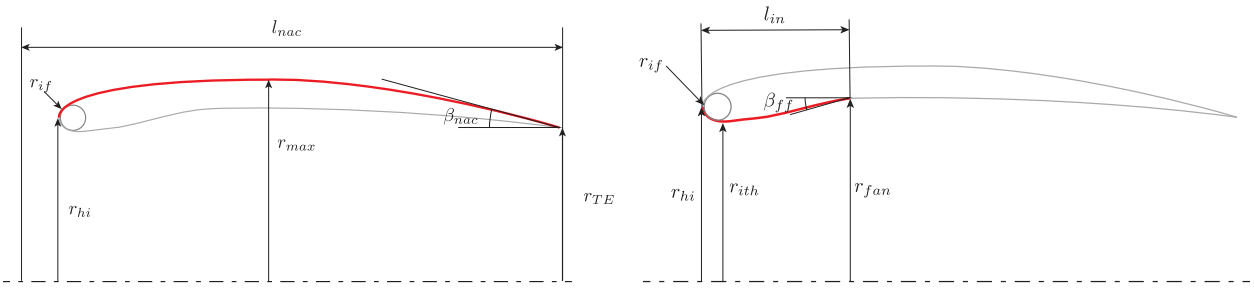

(a) Set of geometry parameters used to define the engine cowling

(b) Set of parameters used to define the geometry of the engine inlet

Figure 8: Engine positioning parameters with respect to the Flying-V

though not optimal, is expected to behave reasonably well for the investigated conditions. The initial parameters used for the geometric model are presented in Table 1.

Table 1: Cowling and inlet parameters that are used to define the geometry of the CRM engine

CRM Cowling		CRM Inlet	
Parameter	Value	Parameter	Value
$r_{\max}$	2.0 m	l_{inlet}	1.1 m
r_{hi}	1.6 m	$f_{\max_{\text{i}}}$	0.2 m
f_{if}	0.38 m	r_{fan}	1.6 m
r_{if}	0.053 m	$r_{\text{inlet}_{\text{th}}}$	1.5 m
l_{nac}	5.97 m	β_{ff}	1.5 deg
r_{te}	1.5 m		
β_{nac}	13.3 deg		

II.F. Mesh Discretization and Computational Method

Once the integrated model is set-up, ParaPy's meshing module is used to generate the grid of the flow field. An unstructured grid of triangles and tetrahedrons is generated following the same approach followed by Faggiano et al. in.[8] Within minutes, this procedure allows to generate a mesh of approximately 2 million elements by just providing a set of input parameters. The laws, based on which the mesh is generated, are parametrized such that regardless of the location or shape of the engine and airframe, the mesh is successfully created automatically. This allows to significantly speed up the modelling process by generating the geometry, and associated mesh of forty different engine positions in just 14 hours on a laptop computer. Even though unstructured meshes are more prone to discretization errors, and it is hard to control the impact that modifying a certain parameter will have on the final mesh, they adapt better to complex geometries and the mesh generation process is usually quicker.

To simulate the aerodynamic behaviour of the Flying-V, both with and without engine a set of CFD Euler simulations are run using the commercial solver ANSYS Fluent. All simulations use a second-order discretization and a pressure-based implicit solver. However, in order to facilitate the convergence of the residuals, the first few hundred iterations are run using a first-order discretization scheme. Also, since the generated meshes are unstructured and composed of tetrahedrons, a Green-Gauss, node-based gradient method is used, as it has been shown to be more accurate and to minimize false diffusion.[18] The simulations are deemed converged when the residuals reach a threshold of $\varepsilon < 10^{-5}$, remain relatively stable, i.e., only variations of $\Delta\varepsilon \sim 10^{-7}$ order are allowed for every 100 iterations, and the lift and drag coefficients have stabilized as well, i.e., only variations of $\Delta\varepsilon \sim 10^{-7}$ order are allowed every 100 iterations.

Thanks to the symmetry of the geometry and the flow conditions assumed here, every simulation is performed using only half of the Flying-V model and imposing a symmetry constraint. All simulations are run

using a rectangular domain ($100c_{\text{ref}}$) as seen in Figure 9, where the recommendations from[19] are followed. On the far-field a pressure boundary is imposed, with cruise conditions according to the International Standard Atmosphere for $h = 13000$ m, $M = 0.85$.

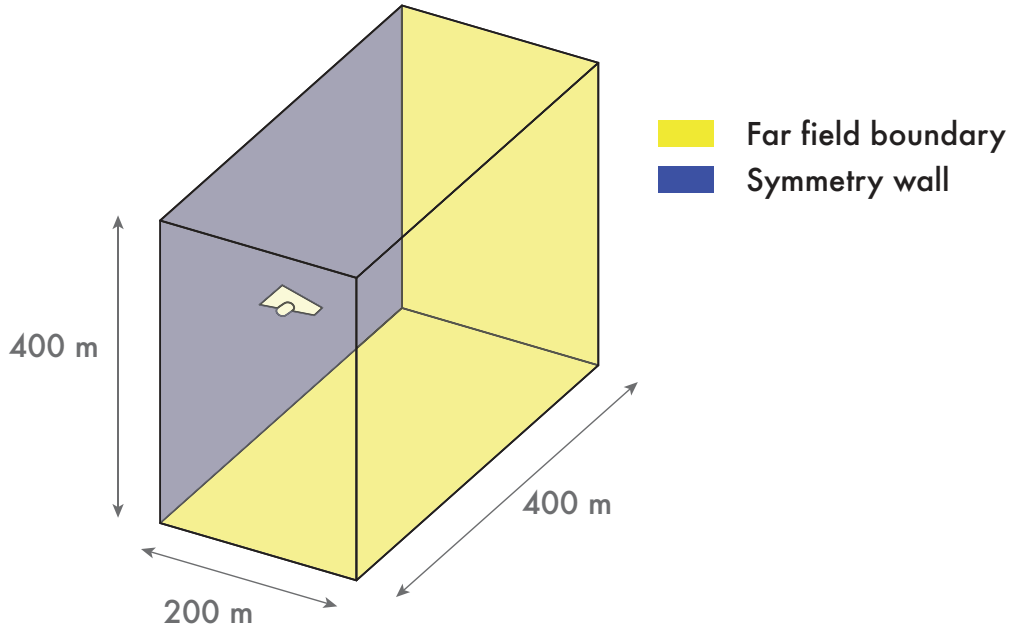

Figure 9: Computational domain used for the engine integration study

Two types of simulations can be distinguished within this work: with the engines behaving as through-flow-nacelles (TFN) and with the engines in powered configuration. The former is generally used in engine-integration studies due to its simplicity and ease of experimental reproducibility.[20] However, TFN simulations cannot reproduce the impact that an operating engine has on the aerodynamics of the real aircraft. For this reason, for every studied position, a more realistic configuration is simulated with powered engines. This is done by modelling the thrust generated in the engine as an additional momentum source term in the x-direction. This extra term needs to be coherent with the Navier Stokes equations, and thus, a subsequent energy source term needs to be added inside the fan area. The following equations govern the increase in linear momentum, S_x and Energy (E):

$$S_x = \frac{\mathrm{T}}{V_f} \tag{16}$$

$$E = S_x \cdot \vec{v}_{\text{ff}} \tag{17}$$

where T represents the engine thrust, V_f the fan volume, $\vec{v}_{\text{ff}}$ the speed at the fan face. Equation 16 can be added as input to the *fan* cell zone if the *source term* option is active. The energy equation, on the contrary, is added with a so called User Defined Function (UDF). The velocity of the flow on every point of the fan face is computed at every instant of the simulation so that the energy added can be accurately calculated. f_{vol} is obtained from ParaPy's *volume attribute* of the fan solid. The thrust for cruise conditions is obtained taking into account the relation $T = D$, where 'D is extracted from the drag coefficient obtained in the preliminary study carried out by Faggiano et al.[8] All this result in an engine thrust of $T = 50$ kN per engine and a fan volume of 0.4 m^3.

II.G. Thrust and Drag Bookkeeping Method

Fluent uses a near-field strategy to compute the forces acting on the bodies under consideration. For this reason, once the horizontal forces acting on the nacelle are computed, they have to be divided between those corresponding to drag, and those which are a consequence of the thrust being generated. Making this subdivision is not trivial, and in this work, a combination of the classical procedure established by AGARD in 1979,[21] and the more recent and simplified approach presented by Heiderbrecht et al. in[16] is used. Thus,

the results obtained are under the assumption that aft- and fore-body cowl forces are independent from each other. It is also assumed that no post-exit forces exist, since the exhaust flow quickly expands towards the ambient pressure. Under this assumption, only the external cowling, and inlet lip pressures are taken into account in terms of drag computations. The main limitation of this approach, though, is that it does not consider the effect of the nozzle. Nevertheless, given the preliminary stage of this integration study, and considering the fact that the nacelle model being used already oversimplifies the shape of the actual engine (especially around the nozzle region) it is believed that this assumption is quite reasonable.

Regarding the computation of the total drag of the installed configuration, the methodology proposed by Stańkowski et al. in[19] is used. A standard, near-field method is applied to the complete aircraft geometry, analogously to the near-field method explained above for the nacelle. Once the drag contribution of each component (airframe, (AF), and nacelle, (nac)) is computed, the interference drag of each of the elements can be obtained by subtracting the drag computations of the isolated components, to the drag of the installed components obtained under the same flow conditions:

$$\Delta D_{\mathrm{AF}} = D_{AF_{\mathrm{installed}}} - D_{AF_{\mathrm{isolated}}}, \tag{18}$$

$$\Delta D_{\mathrm{nac}} = D_{\mathrm{nac}_{\mathrm{installed}}} - D_{\mathrm{nac}_{\mathrm{isolated}}}. \tag{19}$$

Since Euler simulations are run, to account for the contribution of viscosity in the overall performance of the Flying-V, the procedure proposed by Faggiano et al. in their previous study[8] is used to account for the profile drag by computing the skin-friction and pressure contributions as:

$$C_{Df} = C_f \cdot FF \cdot \frac{S_{\mathrm{wet}}}{S}, \tag{20}$$

where C_{F} is the flat plate skin friction coefficient, FF is the form factor of each component (pylon, engine, tail, etcetera), and S, and S_{wet} refer to the reference, and wetted area, respectively. Adding up each of the contributions, the total profile drag is given by:

$$C_{Df} = C_{Df_{\mathrm{wing}}} + C_{Df_{\mathrm{fins}}} + C_{Df_{\mathrm{nacelles}}}, \tag{21}$$

which leads to:

$$L/D = \frac{C_L}{C_{Df} + C_{D_{\mathrm{inv}}}} \tag{22}$$

where $C_{D_textinv}$ is the inviscid drag coefficient obtained from CFD computations.

III. Verification & Validation

The validation of engine-airframe integration CFD simulations with experimental results is, for many reasons, a challenging task. This is not only because of the complexity of the flow field involved, but due to the lack of publicly available experimental results, and specific data. To work around this situation, the verification of the results is performed by comparing them against previous Flying-V studies (without engines), and other analytical approximations which allow to ensure the reliability of the results obtained.

III.A. SU2 vs. Fluent

The past research on this novel design focused on the Flying-V aerodynamic design and brought light into this matter using SU2, an open source solver. Nevertheless, at the moment of carrying out this investigation, SU2 cannot be used to simulate engine-on flight conditions in the manner proposed in Section II. Therefore, ANSYS Fluent is used instead. The first step is to replicate the simulations carried out by Faggiano et al.[8] with ANSYS Fluent. Since the main objective is to determine the impact of the engine position on the lift to drag ratio, it is fundamental to have a baseline lift-to-drag ratio so that the variations encountered can be properly addressed. Hence, to ensure that the results obtained with this study are indeed comparable, the clean Flying-V configuration is run with Fluent using the same setup as for the integrated configuration outlined in.[8]

First, a simulation is run with SU2 using a density based solver as presented in.[8] Subsequently, two additional simulations are run with Fluent: one with a density-based solver, and one with a pressure-based solver. Table 2 presents a comparison between the SU2 results and the Fluent results when using the

density-based solver. Percentage wise, the differences between the lift coefficients are almost negligible, but when comparing just the inviscid drag coefficient obtained with each solver, the discrepancies go as high as 15%. The contrasting results can be attributed to the fact that two different solvers are being used: each makes use of a different discretization. Since the geometry of the Flying V has been optimized with SU2 to obtain minimum inviscid drag at the design lift coefficient, the higher inviscid drag obtained is attributed to the different pressure distribution over the wing, leading to more form drag. It is anticipated that proper (re-shaping) of the wing using Fluent could reduce the inviscid drag to a value closer to the 54 counts that was estimated with SU2.

Table 2: Comparison between Fluent and SU2 lift and drag coefficients at design cruise conditions: h = 13000 m, M = 0.85, and $\alpha = 2.9°$

	Fluent	SU2	Difference (%)
C_L [∼]	0.26	0.26	2.2
C_D [cts]	111	115	3.7
$C_{D_{\text{inv}}}$ [cts]	63	54	15
C_{D_f} [cts]	54	54	0

III.B. Convergence Study

The meshing module in ParaPy allows to modify many different parameters whose combination has a complicated effect on the number of elements and the overall mesh quality. The finest mesh that could be generated with the computational resources available had around 6 million elements, and required circa 10 hours to converge. Since the idea of this investigation is to conduct a battery of simulations and analyse the impact of around 40 different locations, using a coarser mesh is required. Therefore, it was decided to look for a mesh that did not require high computation times while providing accurate enough results such that, compared against finer meshes, the results would not differ significantly. In the end, the chosen mesh differs less than 1% in C_L and 8% in C_D from the finest simulated mesh while taking circa 2.5 hours to converge (represented by the black dots in Figures 10a and 10b).

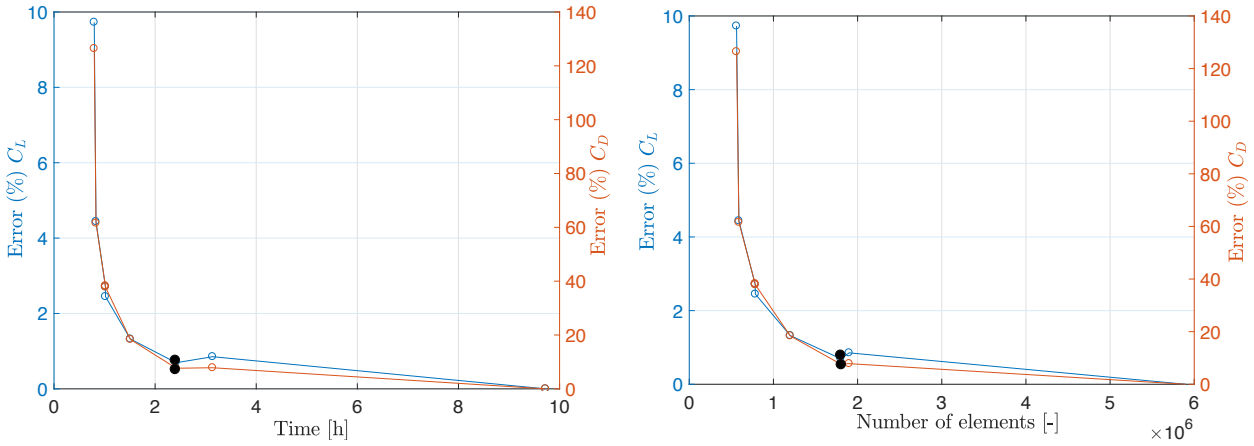

(a) Convergence time for each mesh

(b) Number of mesh elements

Figure 10: ANSYS Fluent grid convergence study for the Flying-V with engines at $h = 13000$ m, $M = 0.85$, and $\alpha = 2.9°$, $T = 50$ kN. Engine Position: $(x,\ y,\ z) = (32.2,\ 7.0,\ 5.6)$ [m]

III.C. Inlet behaviour

The design of the shape of the nacelle is key when doing engine integration studies, as it requires compromises between the internal and external geometry requirements (which are usually conflicting).[22] While the geometry of the nacelle can have a big impact on the aerodynamics of the airframe, it can also greatly affect

the engine performance, as well. How adequate a given engine geometry is, depends both on its interaction with the airframe, and the flight conditions. In this case, the simulations are carried out using the CRM model nacelle, whose geometry was designed for cruise conditions similar to those of the Flying-V. On the Flying-V, however, the nacelle is placed in the vicinity of the suction side of the wing. In the preliminary set of simulations it was observed that the inlet was such that supersonic flow occurred in the diffuser. Obtaining an inlet geometry that optimizes the engine performance was, however, beyond the scope of this project. As a methodological compromise, prior to the simulation of the different engine-airframe configurations the inlet geometry was slightly modified to ensure that the flow going through the engine behaves reasonably for an over-the-wing configuration.

In,[22] Obert explained that, in cruise flight, all design efforts to minimise drag should focus on the reduction of the supervelocities on the engine cowling. The geometry of the inlet, however, also requires some attention, since the throat area concentrates the highest velocities, and the presence of shock waves near the inlet wall needs to be prevented. To achieve so, experience has shown that the average throat Mach number (M_{th}) should be $M_{th} < 0.8$, which can be readily obtained by applying the following equation, which relates M_{th} with the throat area A_{th} and inlet mass flow, assuming one-dimensional flow:

$$A_{th} = \frac{\dot{m}\sqrt{T_T}}{p_T}\left[M_{th}\cdot\left(1+\frac{\gamma-1}{2}\cdot M_{th}^2\right)^{\frac{\gamma+1}{2\cdot(\gamma-1)}}\cdot\sqrt{\frac{\gamma}{R}}\right]^{-1}, \tag{23}$$

where R is the universal gas constant, and T_T and p_T refer to the free-stream total temperature and pressure respectively. Table 3 shows that when applying this relation to the CRM engine geometry with the engine-on condition of $T = 50$ kN, the inlet behaves beyond the recommended threshold, i.e., a throat Mach number of $M_{th} = 0.93$ is obtained, and thus, surpassing the 0.8 limit. In practice, this leads to local supersonic flow inside the intake as the flow is three-dimensional. Figure 11a shows that for the original CRM inlet, the local Mach number distribution on the lower inlet wall increases steadily just before the fan face. This effect causes a large decrease in inlet pressure recovery, and thus, the engine efficiency lowers as well. This behaviour can be overcome by increasing the throat area of the inlet by extending r_{th} until the M_{th} falls below the threshold. Table 3 shows a comparison of the value of M_{th} for different r_{th}. Plotted with the CRM case [see Figure 11a], the two new geometries clearly show a more adequate velocity profile that peaks around the throat and slowly decreases towards the fan face. Thus, preventing the formation of shock waves in that region. Typically, the flow slows down to $M = 0.6$ at the fan face, but in the graphs presented, it remains high even for the modified geometries. This can be due to the fact that the inner geometry of the nacelle needs to be further modified to properly accommodate the incoming flow, since only one out of the six available parameters is modified for this study.

Table 3: M_{th} for the CRM inlet, and the two additional inlet geometries where just the throat radius has been modified at h = 13000 m, M = 0.85, and $\alpha = 2.9°$, $T = 50$ kN

	original CRM	modification 1	modification 2
M_{th}	0.93	0.8	0.75
r_{th} [m]	1.48	1.57	1.61

Figure 11b shows the pressure distribution over the external crown curve of the different nacelles tested. Though the external geometry of the CRM is identical in all cases, modifying the inlet throat radius has an impact on the velocity distribution in the outer surface of the cowling as well. Properly sizing the inlet for the required mass flow reduces the supervelocities present at the leading edge of the original CRM cowling, thus minimising drag. While there is still room for improvement, i.e. a better compromise between the required performance of the external and internal surfaces can be achieved, the presented behavior is considered sufficient for the positioning study of the engine.

IV. Results

To carry out the engine-airframe integration study of the Flying-V, first the aerodynamic behaviour of the separate components is analysed, i.e. airframe and engine, and subsequently, the aerodynamic effects of their interaction are discussed. Then, a preliminary surrogate model is built to help in the selection of a

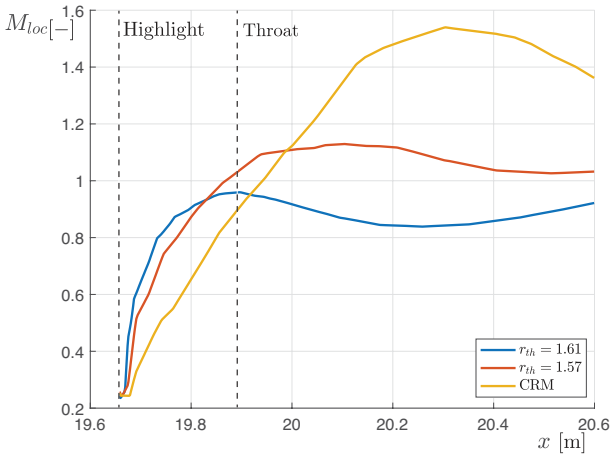

(a) Local Mach number distribution on the lower inlet wall of the Flying-V engines (from highlight up to fan face)

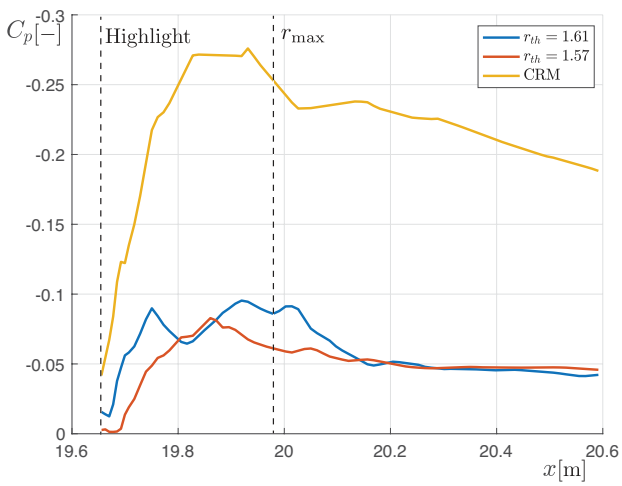

(b) Pressure distribution over the top section of the Flying-V engines (from highlight up to fan face)

Figure 11: Inlet Modification study for $h = 13000$ m, $M = 0.85$, and $\alpha = 2.9°$. Engine Position:$(x,\ y,\ z) = (19.7,\ 3.3,\ 6.1)$ [m]

candidate region for the location of the engine. Finally, a position is recommended on this region by making a trade-off of the different requirements that are being taken into account in this study.

IV.A. Analysis of the Isolated Airframe

The behaviour of this flying wing is further analysed by studying its characteristics at higher angles of attack (up to $\alpha = 10°$). The drag polar of the clean FV is estimated with two objectives in mind: obtaining a benchmark maximum lift-to-drag ratio of the clean configuration using the same solver parameters as for the integrated configuration, and computing the interference drag of the installed configuration for a wide range of angles of attack. Since there are significant differences between the maximum lift-to-drag ratio of the clean and the installed configuration (8%) in conventional aircraft,[20] these preliminary investigations are needed to give an adequate context to the results that follow. Especially, provided the differences observed in Section III, where the mismatch in the drag coefficient between different CFD solvers was highlighted. To do so, the results obtained with Fluent for a set of angles of attack are interpolated to the following drag polar expression:

$$C_D = C_{D_{\min}} + K \cdot (C_L - C_{L_{\min}})^2, \tag{24}$$

where $C_{D_{\min}}$, and $C_{L_{\min}}$ are the minimum drag coefficient, and lift coefficient at minimum drag, respectively. These two parameters along with K are identified using MATLAB's *Curve Fitting Toolbox*.

As can be seen in Figure 12, the drag coefficient is sampled in two ways to construct a drag polar: a course sampling spanning a larger angle-of-attack range and a fine sampling around the angle-of attack where maximum lift-to-drag ratio is encountered. This shows that the parabolic drag polar works well for lift coefficients up to 0.4. However, at higher lift coefficients, possibly due to the formation of strong shock waves at the outer wing, the parabolic drag polar should not be used. Table 4 shows the relevant lift and drag coefficients, along with an analytically obtained maximum lift-to-drag ratio. The values in the row labelled with "Fine fit" form the benchmark for the engine integration studies that follow below. Note that the K of that row corresponds to an Oswald factor of 0.65.

IV.B. Analysis of the Isolated Engine

The study of the isolated engine is carried out using both the original CRM model and the modified CRM with $r_{th} = 1.61$ m. The results obtained corroborate what was already observed: the behaviour of the CRM engine in the Flying-V cruise conditions is quite poor. Figure 13 shows that the cowling drag of the CRM engine is four times higher with the engine-on condition, than the modified one. On the other hand, for the TFN case, the CRM nacelle behaves better, since that was the condition for which it was designed.

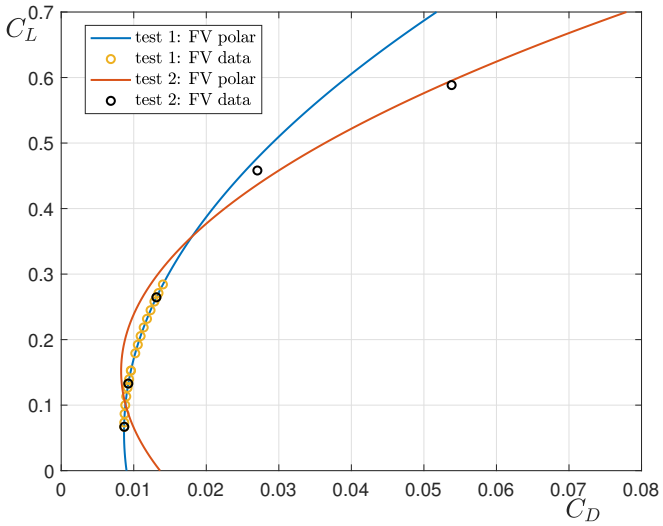

Figure 12: Drag polar estimation of the isolated Flying-V based on the results obtained with Fluent at design cruise conditions: $h = 13000$ m, $M = 0.85$, and $\alpha = 2.9°$

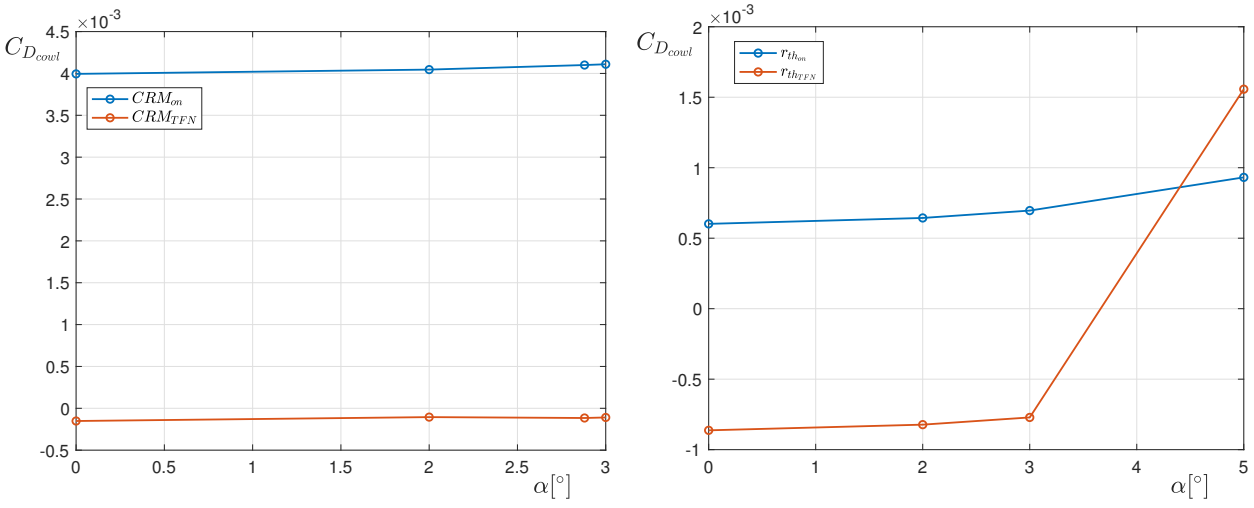

(a) CRM cowling drag

(b) Modified CRM (with $r_{th} = 1.61$ m) cowling drag

Figure 13: Comparison between the cowling drag of the tested engines when working as TFN and in a powered configuration of $T = 50$kN for range of angles of attack at $h = 13000$ m, $M = 0.85$.

Table 4: Polar estimates of the isolated Flying-V based on the results obtained with Fluent at design cruise conditions: $h = 13000$ m, and $M = 0.85$; maximum lift-to-drag ratio obtained with the estimated polar, and confidence of the estimation

	$C_{D\text{min}}$ [cts]	K	$C_{L_{\text{min}}}$	$\left(\frac{C_L}{C_D}\right)_{\text{max}}$	R^2
Coarse fit	76	0.279	0.17	$(26.69)_{cl=0.24}$	0.98
Fine fit	87	0.104	0.058	$(20.24)_{cl=0.29}$	1.0

In the range of angles of attack considered, ($0° \leq \alpha \leq 5°$), the cowling drag remains almost constant up to $\alpha = 3°$, but beyond this value it starts to increase significantly. Since the integration study is set up for cruise conditions at $\alpha = 2.9°$, this should not pose too much of a problem. Furthermore, as the engine is positioned in the flow field of the wing, it is anticipated that its effective angle of attack is even below this value. However, in off-design conditions, this behaviour should be studied in more detail.

IV.C. Analysis of the Engine-Airframe Integration

To understand the effects of engine integration on the Flying-V airframe the test set-up includes forty different engine locations. As expected, the chosen samples provide a reasonable cover of the design space. The analysis process can be summarized as follows: First, a qualitative analysis is carried out by inspecting the results obtained for a few representative locations (ten positions). Then, a more in-depth quantitative analysis where the forty positions are taken into account is performed, along with the second step of the investigation process (the impact of toe angle, β, on the integration results). Finally, a preliminary surrogate model is built to get a better understanding of the possibilities of the engine integration alternatives available.

IV.C.1. Qualitative Analysis of Flow Behaviour

Out of all the positions tested, four samples which allow to explain the main features observed in the flow field are shown in Figure 14 and Figure 15. In light of these results, it is clear that the main interference problem encountered in the installed configuration is due to an increase in the supervelocities when the surfaces of airframe and engine come closer to each other: a low z-coordinate on the nacelle results in a significant disruption of the flow due to the appearance of a strong shock wave between the engine and the wing (see Figures 15a and 15d). Equivalently, a small spanwise coordinate that drives the engine nearer to the symmetry plane, and thus reducing the space between the nacelles of the two engines, makes the flow behave as passing through a convergent-divergent channel (see Figure 14c). Beside the chordwise coordinate of the nacelle, it can be seen that the closer the engine lip is to the airframe trailing edge, the lesser the interference drag is. A good example in which these three effects are simultaneously minimized is presented in Figures 15b and 14b.

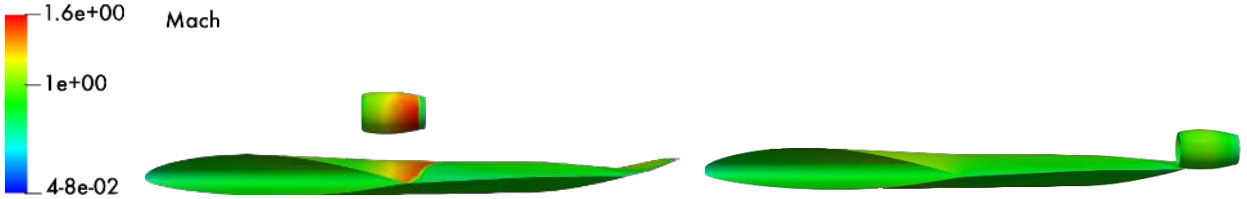

(a) $(x, y, z) = (19.67, 3.34, 6.05)$ m

(b) $(x, y, z) = (45.29, 10.73, 1.97)$ m

(c) $(x, y, z) = (30.80, 2.6, 2.01)$ m

(d) $(x, y, z) = (30.69, 6.51, 3.83)$ m

Figure 14: Side view: comparison among the flow field of various engine location alternatives at h = 13000 m, M = 0.85, $T = 50$ kN, and $\alpha = 2.9°$.

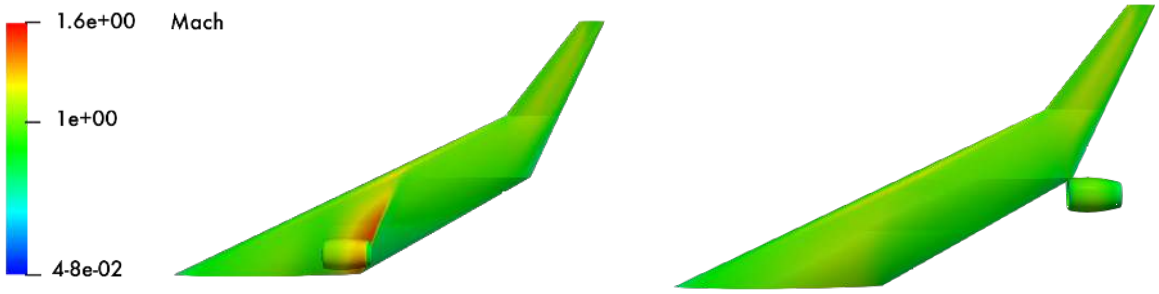

(a) $(x, y, z) = (19.67, 3.34, 6.05)$ m

(b) $(x, y, z) = (45.29, 10.73, 1.97)$ m

(c) $(x, y, z) = (30.80, 2.6, 2.01)$

(d) $(x, y, z) = (30.69, 6.51, 3.83)$ m

Figure 15: Top view: comparison among the flow field of various engine location alternatives at h = 13000 m, M = 0.85, $T = 50$ kN, and $\alpha = 2.9°$.

The highly swept airframe of the Flying-V might pose problems to achieve an adequate engine behaviour, i.e. care needs to be taken so that the flow going through the nacelle is as undisturbed as possible. For this reason, the flow in the surroundings and inner region of the intake is also part of this qualitative analysis. Figure 16 presents a detailed view of the four different positions, where it is possible to appreciate, that the behaviour of the inlet also varies depending on the engine position. The closer the engine is located towards the wing's leading edge, the higher the supervelocities on the outboard side of the inlet lip (see Fig. 16a and 16d). This is explained by the local sideslip angle that is induced by the flow over the highly swept wing. When moving towards the trailing edge in x-direction, the streamlines align more to the freestream direction and the supervelocities on the inner surface of the inlet lip decrease as well (Figures 16c and 16b). Note that with the purpose of better visualizing the flow characteristics, the scale of the legend in Figure 16 has been modified with respect to the one of Figure 15.

IV.C.2. Effect of Position on Aerodynamic Efficiency

Figure 17 shows the lift-to-drag ratio of the aircraft for all the forty positions as a function of the nondimensional coordinates. The results show that misplacing the engine can lead to dramatic lift-to-drag ratio losses, which go as high as 55% when compared against the ideal integration configuration. Out of all the investigated positions, the best and worst alternatives are marked with a green and a red circle respectively, which allows to quickly visualize the trends extracted from the qualitative analysis. Locating the engines too close to the airframe or to the other engine brings along significant interference losses due to the increase of supervelocities in the affected regions. The influence of the ζ coordinate, however, seems to be evenly distributed over the design space. This can be due to several reasons. On the one hand, the design space is parametrized so that the ζ coordinate is always high enough as to allow a proper convergence of the simulations. On the other, the allowed values for ζ are intimately related to the other two coordinates as detailed in Section II. Hence, contrary to intuition, the impact of this parameter on the final result can be significant if the engine is placed on top of the airframe's surface. However, for the design space under consideration here, none of the available ζ locations poses a problem from an aerodynamic point of view. Based on the observed trend, locating the engine as far rearwards as possible yields the highest lift-to-drag

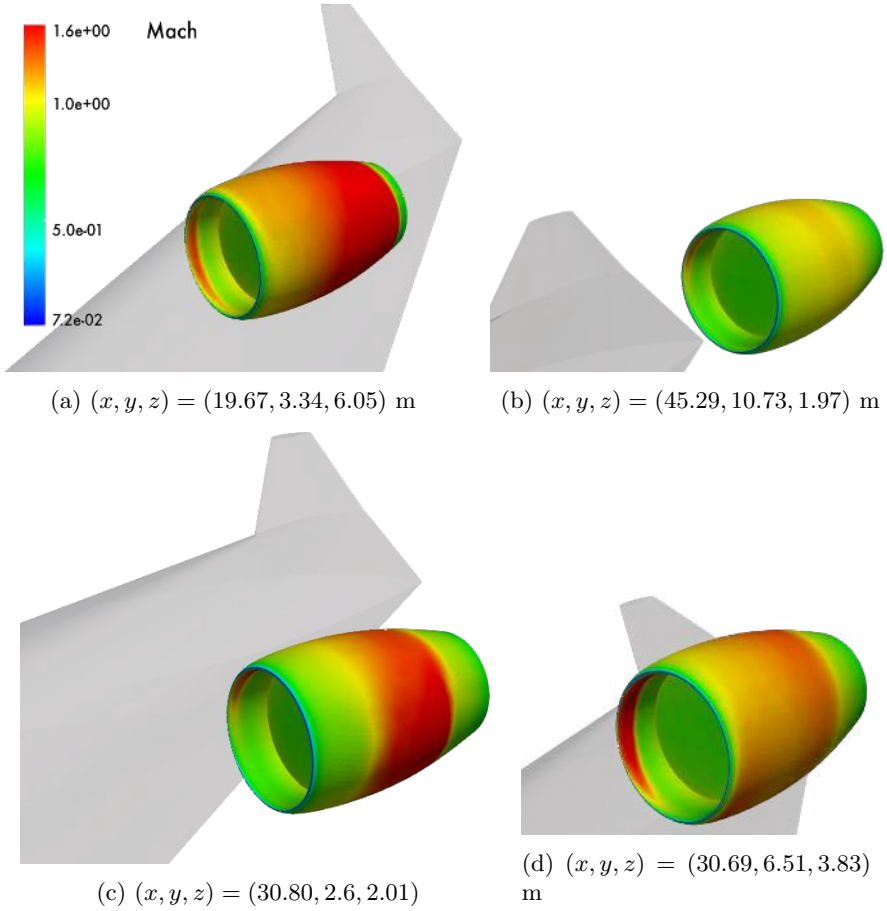

(a) $(x, y, z) = (19.67, 3.34, 6.05)$ m

(b) $(x, y, z) = (45.29, 10.73, 1.97)$ m

(c) $(x, y, z) = (30.80, 2.6, 2.01)$

(d) $(x, y, z) = (30.69, 6.51, 3.83)$ m

Figure 16: Top view: comparison among the flow field of various engine location alternatives at h = 13000 m, M = 0.85, $T = 50$ kN, and $\alpha = 2.9°$.

ratio. To a lesser extent, but still noticeable, further away from the symmetry plane also increases the lift-to drag ratio.

IV.C.3. Effect of Toe Angle on Aerodynamic Efficiency

To better understand the effect that the curvature of the streamlines has on the aircraft efficiency an additional set of experiments is performed for two far-off configurations by modifying the toe-in angle of the nacelles [see Figures 15b, and 15c]. In a real-case scenario, only the orientation of the outer geometry would be modified to keep the thrust aligned with the flight direction. To mimic this set up in a more simplified manner, the nacelle is rotated, but the momentum source added to the fan zone remains in the x-direction.

Figure 18 shows the estimated drag coefficient for both engine positions with different toe angle, β. In the configuration where the engines are located furthest apart (Figure 18b), it is interesting to see whether a change in the toe-in angle can be beneficial due to a more favourable entry angle of the streamlines inside the inlet. On the other hand, in the configuration with the engines close to each other (Figure 18a), it is interesting to test if by changing the shape of the convergent-divergent channel between the two engines the supervelocities in that region can be lowered.

The results obtained show that when the engine is located behind the leading edge of the wing, a change in orientation does not benefit the integration, not only because the resultant drag is higher for all the configurations tested than for the nominal configuration, but also because, in that region, the streamlines have already recovered from the sweep effect, and thus, the intake is no longer aligned with the incoming flow when a certain toe angle is applied. Besides, modifying the toe angle in the region near the symmetry plane does not help diminish the total drag of the configuration either, since the channel formed between engines causes an increase of the supervelocities, regardless of the orientation of the engines.

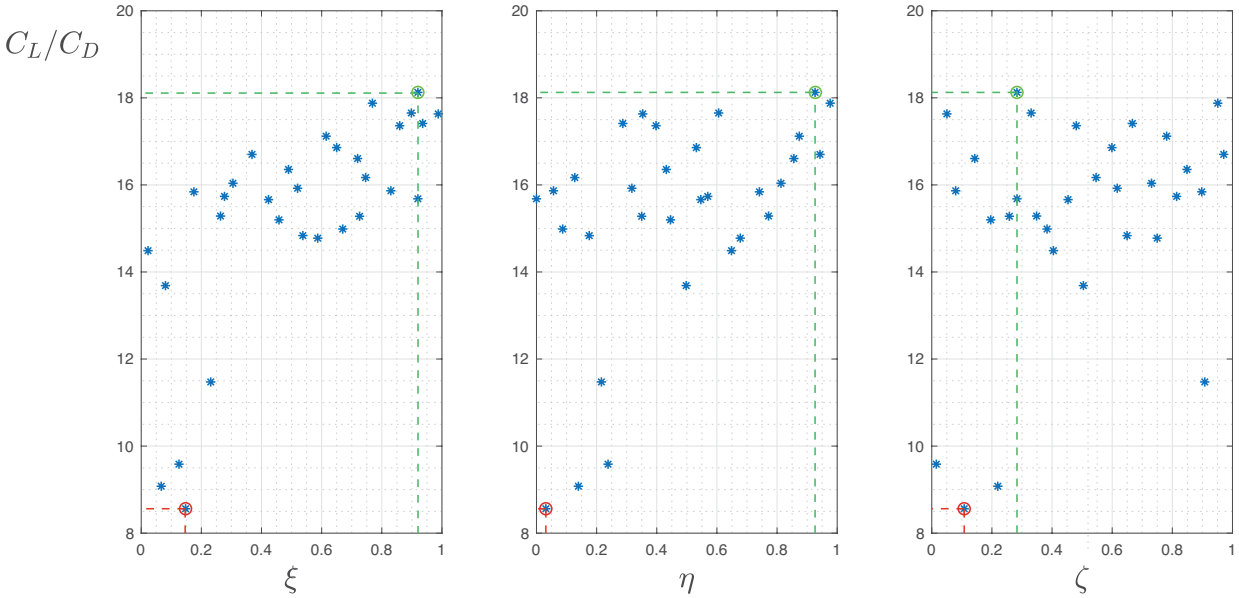

Figure 17: DOE results at h = 13000 m, M = 0.85, $T = 50$ kN, and $\alpha = 2.9°$.

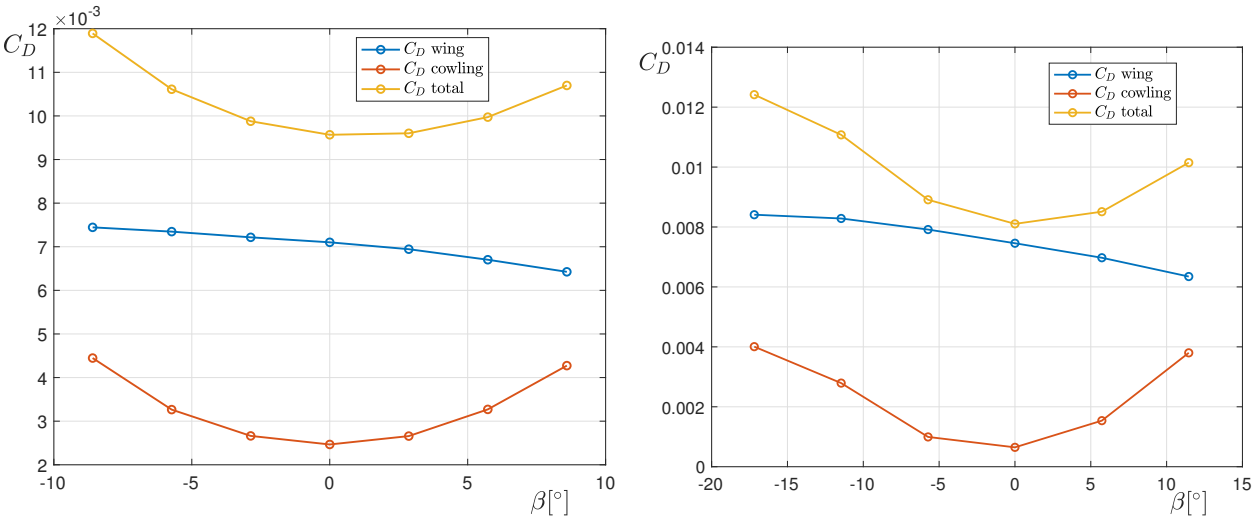

(a) $(x, y, z) = (30.80, 2.6, 2.01)$ m

(b) $(x, y, z) = (30.69, 6.51, 3.83)$ m

Figure 18: Engine orientation influence on the total drag of the integrated configuration at cruise conditions: h = 13000 m, M = 0.85, $T = 50$ kN, and $\alpha = 2.9°$.

IV.D. Surrogate Model

In order to get an overview of the influence of all three coordinates together, and to choose an adequate region to locate the engine, a surrogate model is built from the numerical results. A cubic interpolation scheme with no extrapolation is chosen to perform this. Figure 19 shows three different cuts of the cubic interpolation for different z-planes where the lift-to-drag ratio distribution is shown inside the convex hull of the simulated samples. In light of this visualization, the trend that was observed in previous sections is confirmed: The furthest the engines are located from the wing, and from each other, the higher the lift-to-drag ratio. The surrogate model also shows that the lift-to-drag ratio quickly saturates when moving away from the symmetry plane and outside the airframe. This suggests that there is a wide area behind the outboard region of the wing where the change in lift-to-drag ratio is small and close to the optimum.

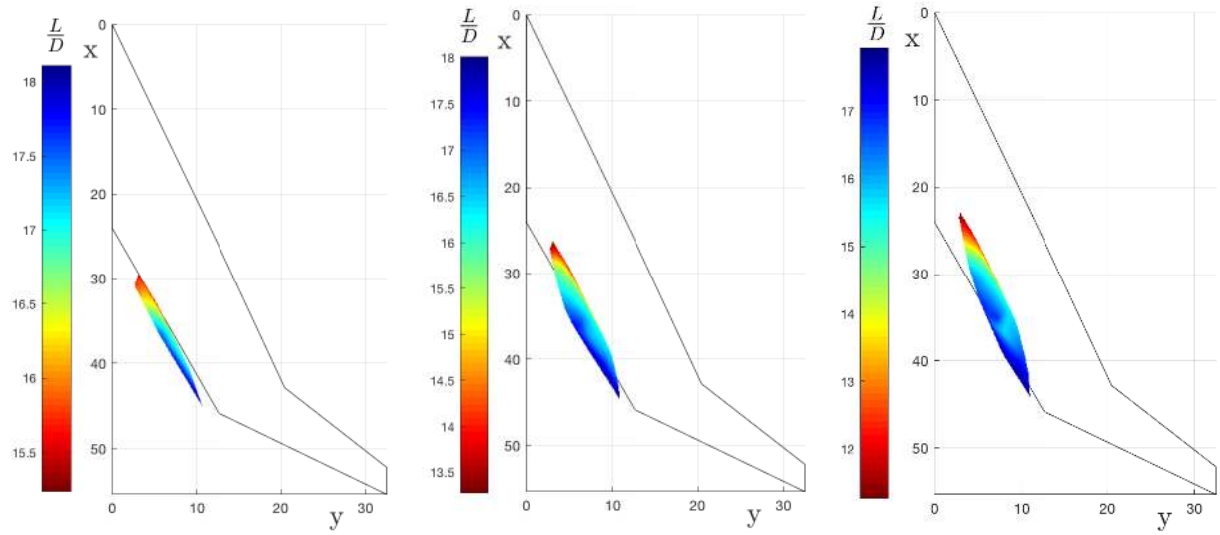

(a) $z = 2$ m (b) $z = 3$ m (c) $z = 4$ m

Figure 19: L/D polynomial regression for the data obtained at cruise conditions: h = 13000 m, M = 0.85, $T = 50$ kN, and $\alpha = 2.9°$ for a fixed z-coordinate of the engine

The existence of such preferred region, allows, from a multidisciplinary perspective, to take into account other factors when deciding where to place the engine without harming too much the aerodynamic efficiency. For instance, placing the engines the furthest apart from each other and the wing would require the use of large structural components, and would be highly demanding for the control surfaces in case of a one-engine-inoperative condition. Plus, it would not be possible to exploit the integration of other heavy components such as the undercarriage under that same structure. Having some design freedom in the optimal aerodynamic positioning of the engine means that the overall optimal location can be set trying to achieve a compromise between these other disciplines

IV.E. Proposed Engine Location

To decide on a feasible area for the engine location, as well as a proposed engine location, all the aspects mentioned up to this point are taken into account. The feasible region proposed is presented in Figure 20, and it covers the region where the figure of merit reaches its maximum value (for the cruise conditions considered in this investigation). Out of all the locations tested, only four points fall in the proposed region. A more comprehensive analysis including several angles of attack (and identical cruise conditions) is performed for one specific engine location which is deemed of interest. This location is shown as a yellow dot in Figure 20. From here on out, it is referred to as the *recommended location*, since it provides a good compromise among the different requirements imposed. The following reasoning is applied to choose this location: within the identified feasible region, most inboard to limit one-engine-inoperative yawing moment, and as low as possible to limit the thrust-induced nose-down pitching moment as well as the structural weight. Also, from a regulatory point of view, the recommended location is deemed safe as the probability of impact falls just below 5% according to the analysis of Section II.

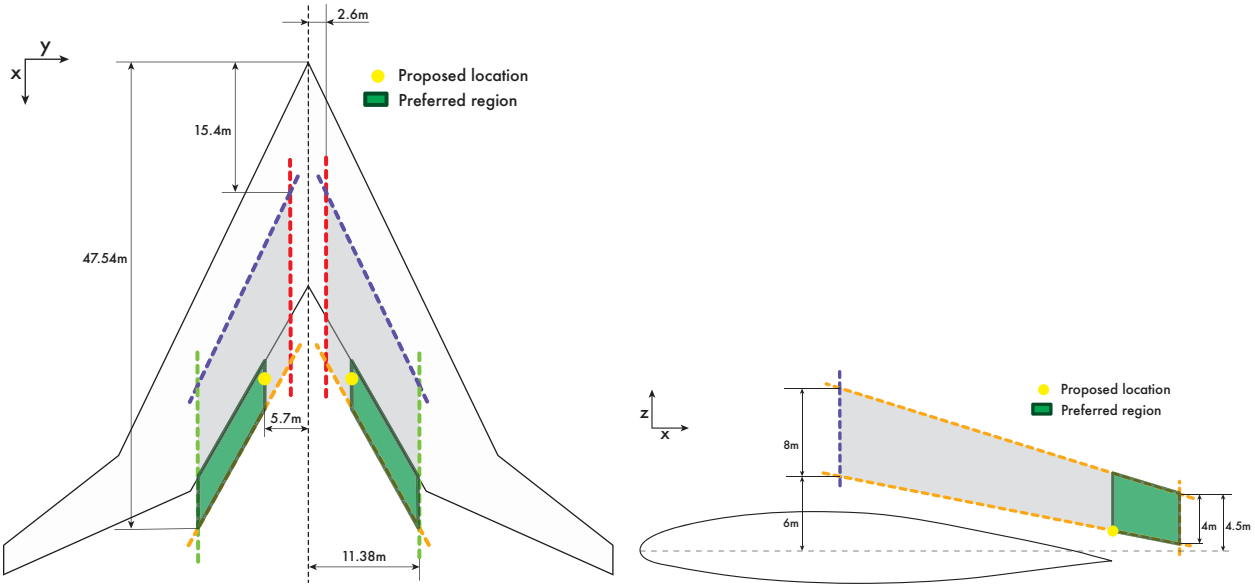

(a) Top view of the proposed engine region

(b) Section-AA of the proposed engine region

Figure 20: Feasible engine region and recommended engine location

Two additional drag polars are produced for the recommended location: one assuming a through-flow nacelle (TFN) and one for a powered configuration with a thrust of $T = 50$ kN. The polars of Figure 21, and the data of Table 5 show that the aerodynamic efficiency of the Flying V is lowered due to the addition of the engines. This is expected as a result of the increase in wetted area and reduces the maximum lift-to-drag ratio obtained. Besides, analogously to what was observed in the CRM engine installation investigations presented in[20] the losses observed when going from a clean to a installed configuration (powered), are near the 10%. The maximum lift-to-drag ratio obtained for a fixed set of cruise conditions is obtained at a higher angle of attack. Also, it is interesting to mention that the performance of the engine-on configuration is significantly better than the one with the TFN, as the additional suction induced by the engine causes a small increase in lift while the boat-tail drag of the cowling is reduced due to the presence of an exhaust.

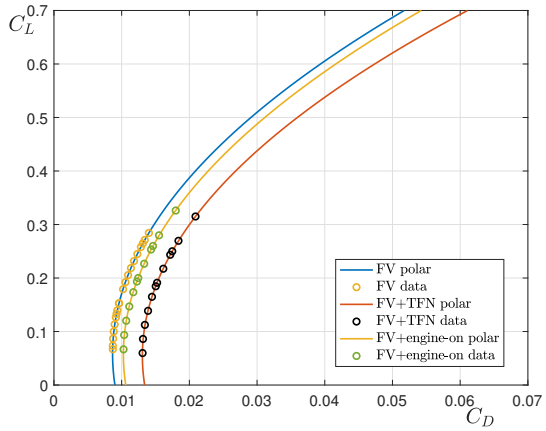

Figure 21: Comparison of the drag polars for the Flying V in clean configuration as well as for and installed configuration at the recommended location. Cruise conditions: $h = 13000$ m, and $M = 0.85$. Engine position $(x,\ y,\ z) = (37.38,\ 5.70\ 0.77)$

Finally, it is fundamental to remark, that when looking at the results obtained, the focus should not be directed to the specific values, but to the perturbations observed on the lift-to-drag ratio after installing the engine. Also, if the flight cruise conditions are modified, these values would vary, but the trends detected in

Table 5: Estimation of the aerodynamic coefficients at design cruise conditions: $h = 13000$ m, and $M = 0.85$.

	$C_{D_{\min}}$ [cts]	K	$C_{L_{\min}}$	$\left(\frac{C_L}{C_D}\right)_{\max}$	R^2
FV	87	0.104	0.058	$(20.24)_{cl=0.29}$	1.000
FV + power on	103	0.106	0.057	$(18.15)_{cl=0.31}$	0.999
FV + TFN	131	0.115	0.054	$(15.12)_{cl=0.33}$	0.999

this investigation would remain unchanged, and thus, the recommended region and location would still be valid.

V. Conclusions & Future Work

The effect of engine location on the aerodynamic efficiency has been studied. It has been shown that the aerodynamic interaction between the airframe and the nacelle, as well as between both nacelles have a large effect on the aerodynamic efficiency of the aircraft: misplacing the engine by locating it too close to the airframe or too close to the symmetry plane can lead to a 55% decrease in lift-to-drag ratio compared to the most optimal position. Based on this study a feasible engine volume is defined, and an engine location is proposed that has a 10% penalty in aerodynamic efficiency, a minimum one-engine-inoperative yawing moment and a small thrust-induced pitching moment.

Based on the results obtained, the work here presented could be further extended into additional lines of investigation: a joint optimization of the geometry of both bodies can be carried out with the aim of maximizing the aerodynamic efficiency of this flying wing configuration and to further reduce the installation penalty. Furthermore, based on the knowledge obtained from this preliminary study, it would be interesting to carry out a more detailed analysis including an adequately designed pylon, and if possible, improve the performance of the installed configuration by exploring innovative engine-airframe integration alternatives. In particular, the recommended location offers the possibility to look into more synergistic proposals, such as, for instance, boundary layer ingestion. Finally, the suitability of the proposed region outside of cruise conditions needs to be evaluated as well.

References

[1]Torenbeek, E., *Synthesis of subsonic airplane design*, Delft Univeristy Press & Martinus Nijhotf Publishers,, 1982.

[2]Wood, R. M. and Bauer, S. X., "Flying Wings / Flying Fuselages," *39th Aerospace Sciences Meeting and Exhibit*, 2001.

[3]R., M.-V., "Flying Wings. A New Paradigm for Civil Aviation?" *Acta Polytechnica*, Vol. 47, No. 1, 2007.

[4]Martinez-Val, R., Palacin, J. F., and Perez, E., "The evolution of jet airliners explained through the range equation," *Proceedings of the Institution of Mechanical Engineers, Part G: Journal of Aerospace Engineering 222*, Vol. 915, 2008.

[5]Benad, J., "The Flying V: A new aircraft configuration for commercial passenger transport," Tech. rep., Deutscher Luft- und Raumfahrtkongress, 2015.

[6]Faggiano, F., *Aerodynamic Design Optimization of a Flying V Aircraft*, Master's thesis, Faculty of Aerospace Engineering, 2016.

[7]van der Schaft, L., *Development, Model Generation and Analysis of a Flying V Structure Concept*, Master's thesis, Delft University of Technology, 2017.

[8]Faggiano, F., Vos, R., Baan, M., and van Dijk, R., "Aerodynamic Design of a Flying V Aircraft," *17th AIAA Aviation Technology, Integration, and Operations Conference*, 2016.

[9]Berry, D. L., "The Boeing 777 Engine/Aircraft Integration Aerodynamics Design Process," *ICAS*, 1994.

[10]Wengiao Gan, Z. Z. and Zhang, X., "Airframe/intake-exhaust integration design of flying wing using a multi-bump strategy," *Proceedings of the Institution of Mechanical Engineers, Part G: Journal of Aerospace Engineering*, 2017.

[11]Bijewitz, J., Seitz, A., and Hornung, M., "A review of recent aircraft concepts employing synergistic propulsion-airframe integration," *30th Congress of the International Council of the Aeronautical Sciences*, 2016.

[12]Carter, M. B., Campbell, R. L., and Serrano, L., "Designing and Testing a Blended Wing Body with Boundary-Layer Ingestion Nacelles," *Journal of Aircraft*, Vol. 43, No. 5, 2006, pp. 1479–1489.

[13]Kok, H., Voskuijl, M., and van Tooren, M., "Distributed Propulsion Featuring Boundary Layer Ingestion Engines for the Blended Wing Body Subsonic Transport," *51st AIAA/ASME/ASCE/AHS/ASC Structures, Structural Dynamics, and Materials Conference; 18th AIAA/ASME/AHS Adaptive Structures Conference; 12th*, 2010.

[14]Lord, W. K., Hendricks, G., Kirby, M., Ochs, S. S., Lin, R.-S., and Hardin, L. W., "Impact of Ultra-High Bypass/ Hybrid Wing Body Integration on Propulsion System Perrformance and Operability (Invited)," *54th AIAA Aerospace Sciences Meeting*, 2016.

[15] "Design Considerations for Minimizing Hazards Caused by Uncontained Turbine Engine and Auxiliary Power Unit Rotor Failure," Advisory circular ac 20-128a 20-128a, Federal Aviation Administration, 1997.

[16] Heidebrecht, A., Stańkowski, T., and MacManus, D., "Parametric Geometry and CFD Process for Turbofan Nacelles," *ASME Turbo Expo 2016: Turbomachinery Technical Conference and Exposition*, Vol. Volume 1: Aircraft Engine; Fans and Blowers; Marine, June 2016.

[17] Christie, R., Heidebrecht, A., and MacManus, D., "An Automated Approach to Nacelle Parameterization Using Intuitive Class Shape Transformation Curves," *Journal of Engineering for Gas Turbines and Power*, January 2017.

[18] ANSYS, Inc, *ANSYS FLUENT 12.0 User's Guide*, April 2009.

[19] Stańkowski, T. P., MacManus, D. G., Sheaf, C. T., and Christie, R., "Aerodynamics of aero-engine installation," *Proceedings of the Institution of Mechanical Engineers, Part G: Journal of Aerospace Engineering*, Vol. 230, No. 14, 2016, pp. 2673–2692.

[20] Stankowski, T. P., MacManus, D. G., Robinson, M., and Sheaf, C. T., "Aerodynamic Effects of Propulsion Integration for High Bypass Ratio Engines," *Journal of Aircraft*, Vol. 54, No. 6, 2017, pp. 2270–2284.

[21] Group, M.-I. D. A. P. M. S., "Guide to In-Flight Trhust Measurement of Turbojects and Fan Engines," AGARDograph 237, Advisory Group for Aerospace Research and Development, January, 1979.

[22] Obert, E., *Aerodynamic Design of Transport Aircraft*, IOS Press BV, 2009.